

Ultrafast self-gating Bragg diffraction of exploding nanocrystals in an X-ray laser

Carl Caleman,^{1,2,6} Nicușor Tîmneanu,^{2,3,6} Andrew V. Martin,^{1,7}
H. Olof Jönsson,² Andrew Aquila,¹ Anton Barty,¹ Howard A. Scott,⁴
Thomas A. White,¹ and Henry N. Chapman^{1,5,*}

¹Center for Free-Electron Laser Science, DESY, Notkestraße 85,
DE-22607 Hamburg, Germany

²Department of Physics and Astronomy, Uppsala University, Box 516,
SE-751 20 Uppsala, Sweden

³Department of Cell and Molecular Biology, Uppsala University, Biomedical Centre,
Box 596, SE-751 24 Uppsala, Sweden

⁴Lawrence Livermore National Laboratory, 7000 East Avenue, Livermore,
California 94550, USA

⁵University of Hamburg, Luruper Chaussee 149, DE-22761 Hamburg, Germany

⁶These authors contributed equally to this work

⁷Present address: ARC Centre of Excellence for Advanced Molecular Imaging, School of
Physics, The University of Melbourne, Victoria, 3010, Australia

*henry.chapman@cfel.de

Abstract: In structural determination of crystalline proteins using intense femtosecond X-ray lasers, damage processes lead to loss of structural coherence during the exposure. We use a nonthermal description for the damage dynamics to calculate the ultrafast ionization and the subsequent atomic displacement. These effects degrade the Bragg diffraction on femtosecond time scales and gate the ultrafast imaging. This process is intensity and resolution dependent. At high intensities the signal is gated by the ionization affecting low resolution information first. At lower intensities, atomic displacement dominates the loss of coherence affecting high-resolution information. We find that pulse length is not a limiting factor as long as there is a high enough X-ray flux to measure a diffracted signal.

© 2015 Optical Society of America

OCIS codes: (140.7240) UV, EUV, and X-ray lasers; (140.7090) Ultrafast lasers; (170.7440) X-ray imaging; (260.1960) Diffraction theory; (320.7120) Ultrafast phenomena.

References and links

1. R. Neutze, R. Wouts, D. van der Spoel, E. Weckert, and J. Hajdu, "Potential for biomolecular imaging with femtosecond X-ray pulses," *Nature* **406**, 752–757 (2000).
2. H. N. Chapman, C. Caleman, and N. Timneanu, "Diffraction before destruction," *Phil. Trans. Roy. Soc. B* **369** (2014).
3. P. Emma, R. Akre, J. Arthur, R. Bionta, C. Bostedt, J. Bozek, A. Brachmann, P. Bucksbaum, R. Coffee, F.-J. Decker, Y. Ding, D. Dowell, S. Edstrom, A. Fisher, J. Frisch, S. Gilevich, J. Hastings, G. Hays, P. Hering, Z. Huang, R. Iverson, H. Loos, M. Messerschmidt, A. Miahnahri, S. Moeller, H.-D. Nuhn, G. Pile, D. Ratner, J. Rzepiela, D. Schultz, T. Smith, P. Stefan, H. Tompkins, J. Turner, J. Welch, W. White, J. Wu, G. Yocky, and J. Galayda, "First lasing and operation of an ångstrom-wavelength free-electron laser," *Nat. Photonics* **4**, 641–647 (2010).
4. H. N. Chapman, P. Fromme, A. Barty, T. A. White, R. A. Kirian, A. Aquila, M. S. Hunter, J. Schulz, D. P. DePonte, U. Weierstall, R. B. Doak, F. R. N. C. Maia, A. V. Martin, I. Schlichting, L. Lomb, N. Coppola, R. L.

- Shoeman, S. W. Epp, R. Hartmann, D. Rolles, A. Rudenko, L. Foucar, N. Kimmel, G. Weidenspointner, P. Holl, M. Liang, M. Barthelmess, C. Caleman, S. Boutet, M. J. Bogan, J. Krzywinski, C. Bostedt, S. Bajt, L. Gumprecht, B. Rudek, B. Erk, C. Schmidt, A. Hoemke, C. Reich, D. Pietschner, L. Strueder, G. Hauser, H. Gorko, J. Ullrich, S. Herrmann, G. Schaller, F. Schopper, H. Soltau, K.-U. Kuehnel, M. Messerschmidt, J. D. Bozek, S. P. Hau-Riege, M. Frank, C. Y. Hampton, R. G. Sierra, D. Starodub, G. J. Williams, J. Hajdu, N. Timneanu, M. M. Seibert, J. Andreasson, A. Rocker, O. Joansson, M. Svenda, S. Stern, K. Nass, R. Andritschke, C.-D. Schroeter, F. Krasniqi, M. Bott, K. E. Schmidt, X. Wang, I. Grotjohann, J. M. Holton, T. R. M. Barends, R. Neutze, S. Marchesini, R. Fromme, S. Schorb, D. Rupp, M. Adolph, T. Gorkhover, I. Andersson, H. Hirsemann, G. Potdevin, H. Graafsma, B. Nilsson, and J. C. H. Spence, "Femtosecond X-ray protein nanocrystallography," *Nature* **470**, 73–78 (2011).
5. L. Lomb, T. Barends, S. Kassemeyer, A. Aquila, S. Epp, B. Erk, L. Foucar, R. Hartmann, B. Rudek, D. Rolles, A. Rudenko, R. Shoeman, J. Andreasson, S. Bajt, M. Barthelmess, A. Barty, M. Bogan, C. Bostedt, J. Bozek, C. Caleman, R. Coffee, N. Coppola, D. DePonte, R. Doak, T. Ekeberg, H. Fleckenstein, P. Fromme, M. Gebhardt, H. Graafsma, L. Gumprecht, C. Hampton, A. Hartmann, G. Hauser, H. Hirsemann, P. Holl, J. Holton, M. Hunter, W. Kabsch, N. Kimmel, R. Kirian, M. Liang, F. Maia, A. Meinhart, S. Marchesini, A. Martin, K. Nass, C. Reich, J. Schulz, M. Seibert, R. Sierra, H. Soltau, J. Spence, J. Steinbrener, F. Stellato, S. Stern, N. Timneanu, X. Wang, G. Weidenspointner, U. Weierstall, T. White, C. Wunderer, H. Chapman, J. Ullrich, L. Struder, and I. Schlichting, "Radiation damage in protein serial femtosecond crystallography using an X-ray free-electron laser," *Phys. Rev. B* **84**, 214111 (2011).
 6. A. Barty, C. Caleman, A. Aquila, N. Timneanu, L. Lomb, T. A. White, J. Andreasson, D. Arnlund, S. Bajt, T. R. M. Barends, M. Barthelmess, M. J. Bogan, C. Bostedt, J. D. Bozek, R. Coffee, N. Coppola, J. Davidsson, D. P. DePonte, R. B. Doak, T. Ekeberg, V. Elser, S. W. Epp, B. Erk, H. Fleckenstein, L. Foucar, P. Fromme, H. Graafsma, L. Gumprecht, J. Hajdu, C. Y. Hampton, R. Hartmann, A. Hartmann, G. Hauser, H. Hirsemann, P. Holl, M. S. Hunter, L. Johansson, S. Kassemeyer, N. Kimmel, R. A. Kirian, M. Liang, F. R. N. C. Maia, E. Malmerberg, S. Marchesini, A. V. Martin, K. Nass, R. Neutze, C. Reich, D. Rolles, B. Rudek, A. Rudenko, H. Scott, I. Schlichting, J. Schulz, M. M. Seibert, R. L. Shoeman, R. G. Sierra, H. Soltau, J. C. H. Spence, F. Stellato, S. Stern, L. Strüder, J. Ullrich, X. Wang, G. Weidenspointner, U. Weierstall, C. B. Wunderer, and H. N. Chapman, "Self-terminating diffraction gates femtosecond X-ray nanocrystallography measurements," *Nat. Photonics* **6**, 35–40 (2012).
 7. S. Boutet, L. Lomb, G. J. Williams, T. R. M. Barends, A. Aquila, R. B. Doak, U. Weierstall, D. P. DePonte, J. Steinbrener, R. L. Shoeman, M. Messerschmidt, A. Barty, T. A. White, S. Kassemeyer, R. A. Kirian, M. M. Seibert, P. A. Montanez, C. Kenney, R. Herbst, P. Hart, J. Pines, G. Haller, S. M. Gruner, H. T. Philipp, M. W. Tate, M. Hromalik, L. J. Koerner, N. van Bakel, J. Morse, W. Ghonsalves, D. Arnlund, M. J. Bogan, C. Caleman, R. Fromme, C. Y. Hampton, M. S. Hunter, L. Johansson, G. Katona, C. Kupitz, M. Liang, A. V. Martin, K. Nass, L. Redecke, F. Stellato, N. Timneanu, D. Wang, N. A. Zatsepin, D. Schafer, J. Defever, R. Neutze, P. Fromme, J. C. H. Spence, H. N. Chapman, and I. Schlichting, "High-resolution protein structure determination by serial femtosecond crystallography," *Science* **337** (2012).
 8. J. Kern, R. Alonso-Mori, J. Hellmich, R. Tran, J. Hattne, H. Laksmono, C. Glöckner, N. Echols, R. G. Sierra, J. Sellberg, B. Lassalle-Kaiser, R. J. Gildea, P. Glatzel, R. W. Grosse-Kunstleve, M. J. Latimer, T. A. McQueen, D. DiFiore, A. R. Fryb, M. Messerschmidt, A. Miahnahri, D. W. Schafer, M. M. Seibert, D. Sokaras, T.-C. Weng, P. H. Zwart, W. E. White, P. D. Adamsa, M. J. Bogan, S. Boutet, G. J. Williams, J. Messinger, N. K. Sauter, A. Zouni, U. Bergmann, J. Yano, and V. K. Yachandra, "Room temperature femtosecond X-ray diffraction of photosystem ii microcrystals," *Proc. Natl. Acad. Sci. U.S.A.* (2012).
 9. L. Redecke, K. Nass, D. P. DePonte, T. A. White, D. Rehders, A. Barty, F. Stellato, M. Liang, T. R. M. Barends, S. Boutet, G. J. Williams, M. Messerschmidt, M. M. Seibert, A. Aquila, D. Arnlund, S. Bajt, T. Barth, M. J. Bogan, C. Caleman, T.-C. Chao, R. B. Doak, H. Fleckenstein, M. Frank, R. Fromme, L. Galli, I. Grotjohann, M. S. Hunter, L. C. Johansson, S. Kassemeyer, G. Katona, R. A. Kirian, R. Koopmann, C. Kupitz, L. Lomb, A. V. Martin, S. Mogk, R. Neutze, R. L. Shoeman, J. Steinbrener, N. Timneanu, D. Wang, U. Weierstall, N. A. Zatsepin, J. C. Spence, P. Fromme, I. Schlichting, M. Duzenko, C. Betzel, and H. N. Chapman, "Natively inhibited trypanosoma brucei cathepsin b structure determined by using an X-ray laser," *Science* **339**, 227–230 (2013).
 10. H. N. Chapman, A. Barty, M. J. Bogan, S. Boutet, M. Frank, S. P. Hau-Riege, S. Marchesini, B. W. Woods, S. Bajt, R. A. London, E. Plönjes, M. Kuhlmann, R. Treusch, S. Düsterer, T. Tschentscher, J. R. Schneider, E. Spiller, T. Möller, C. Bostedt, M. Hoener, D. A. Shapiro, K. O. Hodgson, D. van der Spoel, F. Burmeister, M. Bergh, C. Caleman, G. Huldt, M. M. Seibert, F. R. Maia, R. W. Lee, A. Szöke, N. Timneanu, and J. Hajdu, "Femtosecond diffractive imaging with a soft-X-ray free-electron laser," *Nat. Phys.* **2**, 839–843 (2006).
 11. W. Ackermann, G. Asova, V. Ayvazyan, A. Azima, N. Baboi, J. Baehr, V. Balandin, B. Beutner, A. Brandt, A. Bolzmann, R. Brinkmann, O. I. Brovko, M. Castellano, P. Castro, L. Catani, E. Chiadroni, S. Choroba, A. Cianchi, J. T. Costello, D. Cubaynes, J. Dardis, W. Decking, H. Delsim-Hashemi, A. Delsierys, G. Di Piro, M. Dohlus, S. Duesterer, A. Eckhardt, H. T. Edwards, B. Faatz, J. Feldhaus, K. Floettmann, J. Frisch, L. Froehlich, T. Garvey, U. Gensch, C. Gerth, M. Goerler, N. Golubeva, H.-J. Grabosch, M. Grecki, O. Grimm, K. Hacker, U. Hahn, J. H. Han, K. Honkavaara, T. Hott, M. Huening, Y. Ivanisenko, E. Jaeschke, W. Jalmuzna,

- T. Jezynski, R. Kammering, V. Katalev, K. Kavanagh, E. T. Kennedy, S. Khodyachykh, K. Klose, V. Kocharyan, M. Koerfer, M. Kollwe, W. Koprek, S. Korepanov, D. Kostin, M. Krassilnikov, G. Kube, M. Kuhlmann, C. L. S. Lewis, L. Lilje, T. Limberg, D. Lipka, F. Loehl, H. Luna, M. Luong, M. Martins, M. Meyer, P. Michelato, V. Miltchev, W. D. Moeller, L. Monaco, W. F. O. Mueller, O. Napieralski, O. Napoly, P. Nicolosi, D. Noelle, T. Nunez, A. Oppelt, C. Pagani, R. Paparella, N. Pchalek, J. Pedregosa-Gutierrez, B. Petersen, B. Petrosyan, G. Petrosyan, L. Petrosyan, J. Pflueger, E. Ploenjes, L. Poletto, K. Pozniak, E. Prat, D. Proch, P. Pucyk, P. Radcliffe, H. Redlin, K. Rehlich, M. Richter, M. Roehrs, J. Roensch, R. Romaniuk, M. Ross, J. Rossbach, V. Rybnikov, M. Sachwitz, E. L. Saldin, W. Sandner, H. Schlarb, B. Schmidt, M. Schmitz, P. Schmueser, J. R. Schneider, E. A. Schneidmiller, S. Schnepf, S. Schreiber, M. Seidel, D. Sertore, A. V. Shabunov, C. Simon, S. Simrock, E. Sombrowski, A. A. Sorokin, P. Spanknebel, R. Spesyvtsev, L. Staykov, B. Steffen, F. Stephan, F. Stulle, H. Thom, K. Tiedtke, M. Tischer, S. Toleikis, R. Treusch, D. Trines, I. Tsakov, E. Vogel, T. Weiland, H. Weise, M. Wellhoeffler, M. Wendt, I. Will, A. Winter, K. Wittenburg, W. Wurth, P. Yeates, M. V. Yurkov, I. Zagorodnov, and K. Zapfe, "Operation of a free-electron laser from the extreme ultraviolet to the water window," *Nat. Photonics* **1**, 336–342 (2007).
12. M. M. Seibert, T. Ekeberg, F. R. N. C. Maia, M. Svenda, J. Andreasson, O. Joansson, D. Odic, B. Iwan, A. Rocker, D. Westphal, M. Hantke, D. P. DePonte, A. Barty, J. Schulz, L. Gumprecht, N. Coppola, A. Aquila, M. Liang, T. A. White, A. Martin, C. Caleman, S. Stern, C. Abegg, V. Seltzer, J.-M. Claverie, C. Bostedt, J. D. Bozek, S. Boutet, A. A. Miahnahri, M. Messerschmidt, J. Krzywinski, G. Williams, K. O. Hodgson, M. J. Bogan, C. Y. Hampton, R. G. Sierra, D. Starodub, I. Andersson, S. Bajt, M. Barthelmeß, J. C. H. Spence, P. Fromme, U. Weierstall, R. Kirian, M. Hunter, R. B. Doak, S. Marchesini, S. P. Hau-Riege, M. Frank, R. L. Shoeman, L. Lomb, S. W. Epp, R. Hartmann, D. Rolles, A. Rudenko, C. Schmidt, L. Foucar, N. Kimmel, P. Holl, B. Rudek, B. Erk, A. Hoemke, C. Reich, D. Pietschner, G. Weidenspointner, L. Strueder, G. Hauser, H. Gorke, J. Ullrich, I. Schlichting, S. Herrmann, G. Schaller, F. Schopper, H. Soltau, K.-U. Kuehnel, R. Andritschke, C.-D. Schroeter, F. Krasnig, M. Bott, S. Schorb, D. Rupp, M. Adolph, T. Gorkhover, H. Hirsemann, G. Potdevin, H. Graafsma, B. Nilsson, H. N. Chapman, and J. Hajdu, "Single mimivirus particles intercepted and imaged with an X-ray laser," *Nature* **470**, 78–82 (2011).
 13. M. Bergh, N. Timneanu, and D. van der Spoel, "A model for the dynamics of a water cluster in a X-ray FEL beam," *Phys. Rev. E* **70**, 051904 (2004).
 14. S. P. Hau-Riege, R. A. London, and A. Szöke, "Dynamics of biological molecules irradiated by short X-ray pulses," *Phys. Rev. E* **69**, 051906 (2004).
 15. Z. Jurek, G. Oszlányi, and G. Faigel, "Imaging atom clusters by hard X-ray free-electron lasers," *Europhys. Lett.* **65**, 491–497 (2004).
 16. Z. Jurek, G. Faigel, and M. Tegze, "Dynamics in a cluster under the influence of intense femtosecond hard X-ray pulses," *Eur. Phys. J. D* **29**, 217–229 (2004).
 17. C. Gnodtke, U. Saalman, and J. M. Rost, "Ionization and charge migration through strong internal fields in clusters exposed to intense X-ray pulses," *Phys. Rev. A* **79**, 041201 (2009).
 18. S. Hau-Riege, R. London, G. Huld, and H. Chapman, "Pulse requirements for X-ray diffraction imaging of single biological molecules," *Phys. Rev. E* **71**, 061919 (2005).
 19. S. P. Hau-Riege, "X-ray atomic scattering factors of low-Z ions with a core hole," *Phys. Rev. A* **76**, 042511 (2007).
 20. H. M. Quiney and K. A. Nugent, "Biomolecular imaging and electronic damage using X-ray free-electron lasers," *Nat. Phys.* **7**, 142–146 (2011).
 21. B. E. Warren, *X-Ray Diffraction* (Dover Publications, Inc., 1990).
 22. B. Ziaja, R. A. London, and J. Hajdu, "Unified model of secondary electron cascades in diamond," *J. Appl. Phys.* **97**, 064905 (2005).
 23. C. Caleman, C. Ortiz, E. Marklund, F. Bultmark, M. Gabrysch, F. G. Parak, J. Hajdu, M. Klintonberg, and N. Timneanu, "Radiation damage in biological material: electronic properties and electron impact ionization in urea," *Europhys. Lett.* **85**, 18005, and erratum 88:29901 (2009).
 24. C. Caleman, M. Bergh, H. A. Scott, J. C. H. Spence, H. N. Chapman, and N. Timneanu, "Simulations of radiation damage in biomolecular nanocrystals induced by femtosecond xfel pulses," *J. Mod. Opt.* **58**, 1486–1497 (2011).
 25. J. A. Cowan and C. Nave, "The optimum conditions to collect X-ray data from very small samples," *J. Sync. Rad.* **15**, 458–462 (2008).
 26. C. Nave and M. A. Hill, "Will reduced radiation damage occur with very small crystals?" *J. Sync. Rad.* **12**, 299–303 (2005).
 27. C. Caleman, G. Huld, C. Ortiz, F. R. N. C. Maia, F. G. Parak, J. Hajdu, D. van der Spoel, H. N. Chapman, and N. Timneanu, "On the feasibility of nanocrystal imaging using intense and ultrashort X-ray pulses," *ACS Nano* **5**, 139–146 (2011).
 28. S. P. Hau-Riege, A. Graf, T. Döppner, R. A. London, J. Krzywinski, C. Fortmann, S. H. Glenzer, M. Frank, K. Sokolowski-Tinten, M. Messerschmidt, C. Bostedt, S. Schorb, J. A. Bardley, A. Lutman, D. Rolles, A. Rudenko, and B. Rudbek, "Ultrafast transitions from solid to liquid and plasma states of graphite induced by X-ray free-electron laser pulses," *Phys. Rev. Lett.* **108**, 217402 (2012).
 29. R. Owen, E. Rudino-Pinera, and E. Garman, "Experimental determination of the radiation dose limit for cry-

- oocooled protein crystals," *Proc. Natl. Acad. Sci. U. S. A.* **103**, 4912–4917 (2006).
30. R. Henderson, "The potential and limitations of neutrons, electrons and X-rays for atomic resolution microscopy of unstained biological molecules," *Q. Rev. Biophys.* **28**, 171–193 (1995).
 31. J. M. Holton, "A beginner's guide to radiation damage," *J. Synchr. Rad.* **16**, 133–142 (2009).
 32. C. Caleman, N. Timneanu, A. V. Martin, T. A. White, H. A. Scott, A. Barty, A. Aquila, and H. N. Chapman, "Modeling of XFEL induced ionization and atomic displacement in protein nanocrystals," in "X-Ray Free-Electron Lasers: Beam Diagnostics, Beamline Instrumentation, and Applications," *Proc. SPIE* vol. 8504, S. P. Moeller, M. Yabashi, S. P. Hau-Riege, eds.
 33. J. Andreasson, B. Iwan, A. Andrejczuk, E. Abreu, M. Bergh, C. Caleman, A. J. Nelson, S. Bajt, J. Chalupsky, H. N. Chapman, R. R. Fäustlin, V. Hajkova, P. A. Heimann, B. Hjörvarsson, L. Juha, D. Klinger, J. Krzywinski, B. Nagler, G. K. Pålsson, W. Singer, M. M. Seibert, R. Sobierajski, S. Toleikis, T. Tschentscher, S. M. Vinko, R. W. Lee, J. Hajdu, and N. Timneanu, "Saturated ablation in metal hydrides and acceleration of protons and deuterons to keV energies with a soft-X-ray laser," *Phys. Rev. E* **83**, 016403 (2011).
 34. B. Iwan, J. Andreasson, E. Abreu, M. Bergh, C. Caleman, J. Hajdu, and N. Timneanu, "Modeling of soft X-ray induced ablation in solids," in "Damage to VUV, EUV, and X-Ray Optics III," *Proc. SPIE* vol. 8077, L. Juha, S. Bajt, and R. A. London, eds.
 35. M. Bergh, N. Timneanu, S. P. Hau-Riege, and H. A. Scott, "Interaction of ultrashort X-ray pulses with B₄C, SiC, and Si," *Phys. Rev. E* **77**, 026404 (2008).
 36. M. Bergh, G. Huldt, N. Timneanu, F. R. N. C. Maia, and J. Hajdu, "Feasibility of imaging living cells at sub-nanometer resolutions by ultrafast X-ray diffraction," *Q. Rev. Biophys.* **41**, 181–204 (2008).
 37. H. A. Scott and R. W. Mayle, "GLF- a simulation code for X-ray lasers," *Appl. Phys. B* **58**, 35 (1994).
 38. H. A. Scott, "Cretin-a radiative transfer capability for laboratory plasmas," *J. Quant. Spectrosc. Radiat. Transf.* **71**, 689 (2001).
 39. J. Rubiano, R. Florido, C. Bowen, R. W. Lee, and Y. Ralchenko, "Review of the 4th nlte code comparison workshop," *High Energy Density Phys.* **3**, 225–232 (2007).
 40. R. More, "Electronic energy-levels in dense plasmas," *J. Quant. Spectrosc. Radiat. Transf.* **27**, 345 (1982).
 41. B. Henke, E. Gullikson, and J. Davis, "X-ray interactions: Photoabsorption, scattering, transmission and reflection at E=50–30 000 eV, Z=1–92," *Atom. Nucl. Data Tabl.* **54**, 181 (1993).
 42. L. Spitzer, *Physics of Fully Ionized Gases* (Interscience Publishers, 1956).
 43. D. Gericke, M. S. Murillo, and M. Schlages, "Dense plasma temperature equilibration in the binary collision approximation," *Phys. Rev. E* **65**, 036418 (2002).
 44. J. C. Stewart and K. D. Pyatt, "Lowering of ionization potentials in plasmas," *Astrophys. J.* **144**, 1203 (1966).
 45. M. Nantel, G. Ma, S. Gu, C. Y. Côté, J. Itatani, and D. Umstadter, "Pressure ionization and line merging in strongly coupled plasmas produced by 100-fs laser pulses," *Phys. Rev. Lett.* **80**, 4442–4445 (1998).
 46. S. P. Hau-Riege, "Photoelectron dynamics in X-ray free-electron-laser diffractive imaging of biological samples," *Phys. Rev. Lett.* **108**, 238101 (2012).
 47. S. P. Hau-Riege, H. N. Chapman, J. Krzywinski, R. Sobierajski, S. Bajt, R. A. London, M. Bergh, C. Caleman, R. Nietubyc, L. Juha, J. Kuba, E. Spiller, S. Baker, R. Bionta, K. S. Tinten, N. Stojanovic, B. Kjørnattanawanih, E. Gullikson, E. Plonjes, S. Toleikis, and T. Tschentscher, "Subnanometer-scale measurements of the interaction of ultrafast soft X-ray free-electron-laser pulses with matter," *Phys. Rev. Lett.* **98**, 145502 (2007).
 48. H. N. Chapman, S. P. Hau-Riege, M. J. Bogan, S. Bajt, A. Barty, S. Boutet, S. Marchesini, M. Frank, B. W. Woods, W. H. Benner, R. A. London, U. Rohner, A. Szoke, E. Spiller, T. Moller, C. Bostedt, D. A. Shapiro, M. Kuhlmann, R. Treusch, E. Plonjes, F. Burmeister, M. Bergh, C. Caleman, G. Huldt, M. M. Seibert, and J. Hajdu, "Femtosecond time-delay X-ray holography," *Nature* **448**, 676–679 (2007).
 49. M. M. Seibert, S. Boutet, M. Svenda, T. Ekeberg, F. R. N. C. Maia, M. J. Bogan, N. Timneanu, A. Barty, S. Hau-Riege, C. Caleman, M. Frank, H. Benner, J. Y. Lee, S. Marchesini, J. W. Shaevitz, D. A. Fletcher, S. Bajt, I. Andersson, H. N. Chapman, and J. Hajdu, "Femtosecond diffractive imaging of biological cells," *J. Phys. B: At. Mol. Opt. Phys.* **43**, 194015 (2010).
 50. J. D. Bozek, "AMO instrumentation for the LCLS X-ray FEL," *Eur. Phys. J.-Spec. Top.* **169**, 129–132 (2009).
 51. S.-K. Son, H. N. Chapman, and R. Santra, "Multiwavelength anomalous diffraction at high X-ray intensity," *Phys. Rev. Lett.* **107**, 218102 (2011).
 52. S.-K. Son, H. N. Chapman, and R. Santra, "Determination of multiwavelength anomalous diffraction coefficients at high X-ray intensity," *J. Phys. B* **46**, 164015 (2013).
 53. J. Chalupský, L. Juha, J. J. Cihelka, V. Hájková, S. Koptyaev, J. Krása, A. Velyhan, M. Bergh, C. Caleman, J. Hajdu, R. M. Bionta, H. Chapman, S. P. Hau-Riege, R. A. London, M. Jurek, J. Krzywinski, R. Nietubyc, J. B. Pelka, R. Sobierajski, J. M. ter Vehn, A. Tronnier, K. Sokolowski-Tinten, N. Stojanovic, K. Tiedtke, S. Toleikis, T. Tschentscher, H. Wabnitz, and U. Zastra, "Characteristics of focused soft X-ray free-electron laser beam determined by ablation of organic molecular solids," *Opt. Express* **15**, 6036–6043 (2007).
 54. S. P. Hau-Riege, R. A. London, R. M. Bionta, M. A. McKernan, S. L. Baker, J. Krzywinski, R. Sobierajski, R. Nietubyc, J. B. Pelka, M. Jurek, L. Juha, J. Chalupský, J. Cihelka, V. Hájková, A. Velyhan, J. Krása, J. Kuba, K. Tiedtke, S. Toleikis, T. Tschentscher, H. Wabnitz, M. Bergh, C. Caleman, K. Sokolowski-Tinten, N. Stojanovic, and U. Zastra, "Damage threshold of inorganic solids under free-electron-laser irradiation at 32.5 nm

- wavelength,” *Appl. Phys. Lett.* **90**, 173128 (2007).
55. S. P. Hau-Riege, R. A. London, R. M. Bionta, D. Ryutov, R. Soufli, S. Bajt, M. A. McKernan, S. L. Baker, J. Krzywinski, R. Sobierajski, R. Nietubyc, D. Klinger, J. B. Pelka, M. Jurek, L. Juha, J. Chalupský, J. Cihelka, V. Hájková, A. Velyhan, J. Kársa, K. Tiedtke, S. Toleikis, H. Wabnitz, M. Bergh, C. Caleman, and N. Timneanu, “Wavelength dependence of the damage threshold of inorganic materials under extreme-ultraviolet free-electron-laser irradiation,” *Appl. Phys. Lett.* **95**, 111104 (2009).
 56. M. Harbst, T. N. Hansen, C. Caleman, W. K. Fullagar, P. Jonsson, P. Sondhaus, O. Synnnergren, and J. Larsson, “Studies of resolidification of non-thermally molten insb using time-resolved X-ray diffraction,” *Appl. Phys. A* **81**, 893–900 (2005).
 57. P. Jordan, P. Fromme, H. Witt, O. Klukas, W. Saenger, and N. Krauss, “Three-dimensional structure of cyanobacterial photosystem I at 2.5 angstrom resolution,” *Nature* **411**, 909–917 (2001).
 58. E. A. Schneidmiller and M. V. Yurkov, in “Photon beam properties at the European XFEL,” (XFEL.EU TN-2011-006, Hamburg, 2011).
 59. A. P. Mancuso, in “Conceptual Design Report Scientific Instrument Single Particles, Clusters, and Biomolecules (SPB),” (XFEL.EU TR-2011-007, Hamburg, 2012).
 60. D. L. Book, “NRL (Naval Research Laboratory) Plasma Formulary, Revised,” (2007).
 61. J. A. Ibers and W. C. Hamilton, eds., *International Tables for X-Ray Crystallography* (Kynoch, 1974), vol. 4.
 62. D. T. Cromer and J. B. Mann, “X-ray scattering factors computed from numerical Hartree-Fock wave functions,” *Acta Cryst. A* **24**, 321–326 (1968).
-

1. Introduction

Much of what we know about the detailed structure of proteins has come through the use of X-ray diffraction from macromolecular crystals. Synchrotron radiation has revolutionized this field, enabling studies of larger and more complex systems at increasingly high resolution on smaller (often micron-sized) crystals. The key to this success has been the use of Bragg diffraction from multiple copies of oriented molecules in a single crystal. However, there are classes of proteins (as well as many other types of materials) that are difficult or impossible to crystallize, including membrane proteins and many glycoproteins, for which a high resolution means of structure determination would be invaluable [1, 2].

X-ray Free Electron Lasers (XFEL), such as the Linac Coherent Light Source (LCLS) at the SLAC National Accelerator Laboratory [3], generate short (femtosecond), intense (up to 10^{13} photons per pulse) X-ray pulses. Serial femtosecond crystallography (SFX) takes advantage of these unique properties and has proven to be a technique to get interpretable diffraction images of protein crystals that are too small to be suitable for conventional synchrotron experiments [4–9]. This “diffraction before destruction” [10] technique has been demonstrated both at the soft XFEL in Hamburg, (FLASH) [11] and at LCLS [4–6, 12].

The key to overcoming radiation damage when using this method to image single particles (such as a single protein, cell or virus), is to capture an image before significant motion of the atoms induced by the heavy ionization and explosion of the sample occurs [1, 13–17]. Early theoretical studies have indicated that to be able to image a single protein in vacuum to Ångström resolution, the X-ray pulse length would have to be less than 10 fs [18]. With this goal in mind, X-ray lasers are developing towards flash pulses with high photon flux and short lengths.

In any sample, the ionization due to X-rays occurs at random atomic positions, modifying atomic scattering factors [19, 20]. Bombarding molecules with X-rays ionizes the atoms, causing the molecular bonds to break and producing changes in the structure of the molecules. In a crystalline sample the ionization is spread out among a large number of individual molecules, which reduces the diffracted signal that depends on the correlated part of the structure. The ionizations lead to both a resolution-dependent reduction in Bragg signal and the addition of uniform diffuse scattering (due to the uncorrelated component of the structure) [21]. In an XFEL experiment, the photon bombardment can be so severe that the direct photoionizations and secondary ionizations destroy the sample within the pulse length (typically 10–500 fs). At 2 keV photon energy each single photoionization will generate more than 100 secondary elec-

trons in a biological sample. These secondaries are typically generated within a few femtoseconds [22–24]. Due to their high energy the electrons spread out throughout the crystal causing further ionization, over volumes as large as hundreds of nanometers in diameter [25,26]. In addition, the low energy Auger electrons which result from the Auger decay of the photoionized atom (typically 250–500 eV) give more localised (tens of nanometer) secondary ionizations [27].

Two recent experimental studies [6, 28] described a novel mechanism in ultrafast, ultra-intense X-ray experiments that allows structural information to be collected from crystalline samples using radiation doses considerably higher than the tolerable doses for cryogenically cooled crystals exposed at synchrotron sources [29–31], without the requirement for the pulse to terminate before the onset of sample damage. The diffracted X-rays are gated by the loss of crystalline periodicity, generating a Bragg diffracted pulse with a length significantly shorter than the duration of the actual incident pulse. The present study describes how the pulse integrated diffraction from a protein crystal (using a model system of photosystem I, PSI) depend on atomic displacement and the loss of scattering power, for several photon energies in the range of 2 keV–12 keV and intensities in the range of 10^{17} – 10^{20} W/cm², relevant for experiments at LCLS and future XFEL sources.

2. Simulations and plasma modeling

As in earlier studies [6, 24, 32–36] we simulate the interaction between the XFEL beam and various samples using the non-local thermodynamics equilibrium (non-LTE) radiation transfer code CRETIN [37, 38]. CRETIN is a well-established code in the field of collisional radiative modeling [39]. The code calculates the electronic level populations and transition rates, and generates opacities, heating rates and other material properties as a function of time during the simulation. CRETIN includes a screened hydrogenic atomic model which can be used for many elements as described in [40]. The cold opacities for the light atoms (H, C, N, O and S) generated from the hydrogenic model, are comparable to the Henke absorption coefficients [41] at the relevant photon energies. The electron and ion energy distributions are assumed to be thermal, implying that the electrons thermalize instantaneously. The electron-ion coupling coefficient is calculated with Spitzer's formula [42], using a Coulomb logarithm introduced in [43] for dense systems. The high density of the plasma (here at solid density) leads to a lowering of the continuum edges governed by the Stewart-Pyatt formula [44], a common approximate approach which has been tested against both experiments and more detailed models [45].

The non-LTE code has the advantage that it treats the plasma as a continuum and so it is not limited by the size of the molecular system. This allows the treatment of large systems such as protein crystals at reasonable computational costs, as the computing time scales mainly with the number of computational cells (zones) on which the sample is divided. The tradeoff is that the simulation contains no structural information about the samples. The simulation provides statistical quantities of the system, including ion and electron temperatures and average ion displacements. In the type of samples studied here, protein crystals 700 nm in size, the plasma model is expected to describe the physics well. For smaller systems such as single proteins or viruses in the gas phase, the plasma description is more problematic due to the escape of photoelectrons, or secondary electrons. In such cases a molecular dynamics description [1, 27] or so called hybrid models [46] are more suited. CRETIN also models hydrodynamic volume changes, i.e. expansion and compression due to thermal changes. In an earlier study we have shown that hydrodynamic expansion is small on the femtosecond time scale for the pulse parameters that we are investigating here and can be disregarded [24].

The non-LTE continuum description has proven to agree well with experimental measurements [33, 35, 47–49] at the FLASH free-electron laser in Hamburg, operating in the soft X-ray

regime, at photon energies 39–192 eV. We have also shown that ion displacements from our simulations agree with observations from experiments at the Atomic, Molecular and Optical experimental station (AMO) [50] at LCLS, using 2 keV photons [6].

Simulating the response of a solid, in our case a protein crystal, using a plasma approach is reasonable only if the system has an internal energy that is high enough to consider all chemical bonds as being broken. In practice this means the average ion temperature must be higher than the binding energies in the system. The carbon-carbon binding energy in a neutral system is around 1 eV (corresponding to 100 kJ/mol or a dose in a typical protein of 100 kGy). In the simulations described here, the ion temperature is higher than 1 eV during most of the X-ray exposure. In cases with very low ionization the plasma description is problematic. The ion temperatures are displayed in the Appendix. In the current approach we do not take into account any coherence effects that could occur during rapid ionization of heavy atoms, that could be exploited to determine the location of these particular atomic species [51, 52].

In this study we simulate processes at times scales up to 500 fs, as this is the scale for the longest XFEL pulses that can be produced at LCLS without severe loss in photon flux. At longer time scales, processes not included in the present model would have to be considered, such as vaporization [48], ablation in bulk solids (on nanoseconds time scales) [53–55] and even resolidification (100 ns time scales) [56].

We use a Photo System I (PSI) protein complex crystal, with a width of 700 nm, as our simulation system. PSI [57] is a membrane protein that we have used in earlier studies to demonstrate the feasibility of femtosecond X-ray protein nanocrystallography [4, 6]. The relative atomic content of the crystal was assumed to be $\text{H}_{141,400}\text{O}_{57,300}\text{C}_{16,900}\text{N}_{3,310}\text{S}_{89}\text{Fe}_{12}\text{Mg}_{96}\text{P}_3\text{Ca}$, corresponding to the average composition of a PSI crystal containing 78% water as solvent. For the simulations we have used a crystal of a density of 1.077 g/cm^3 . The simulation geometry is one dimensional, along the direction of the incident laser (similar to that illustrated in [34]). The crystal is divided into equally sized one-dimensional zones. The simulations follow the radiation transfer and electron thermal conduction between adjacent zones, as the radiation propagates through the crystal. The other two transverse dimensions are considered large enough to be treated with periodic boundaries. This is a good approximation for radiation and heat transport in the transverse dimensions, under the assumption that the size of the crystal is smaller than the XFEL focus.

We simulate four different photon energies; 2 keV, 6 keV, 9 keV and 12 keV, which are relevant both for the currently operating LCLS, and the upcoming European XFEL [58]. To span a large set of beam intensities we have simulated flat top pulses with 5×10^4 – $5 \times 10^7\text{ J/cm}^2$ in a 500 fs pulse, corresponding to intensities of 10^{17} – 10^{20} W/cm^2 . These represent the intensities that are available at the LCLS today at the various experimental stations and could be expected using the $0.1\text{ }\mu\text{m}$ diameter focus at the scientific instrument Single Particles, Clusters, and Biomolecules (SPB) at European XFEL [59].

The simulations give ion and electron temperatures and average ionization. Figure 1 shows the average ionization of carbon atoms as a function of time during the pulse, together with a parameter fit. Note that a law of the form t^m does not seem to be universal across our fitting range. Rather, the average ionization, here denoted as \bar{z} , exhibits two regions, one of accelerated ionization ($\bar{z} \sim t^2$) on the short time scales, and one with a decelerated ionization towards saturation ($\bar{z} \sim t^{1/2}$) on longer time scales. The accelerated phase is connected to the secondary ionization cascades which quickly enhance ionization, and this has been described earlier [27].

To estimate the atomic disorder and how it reduces the Bragg signal, we consider at the ion motion inside a plasma. Electrons heat the ions up through collisions, however most of the ion motion comes from ion-ion collisions. We calculate the diffusion coefficient D_i , which from

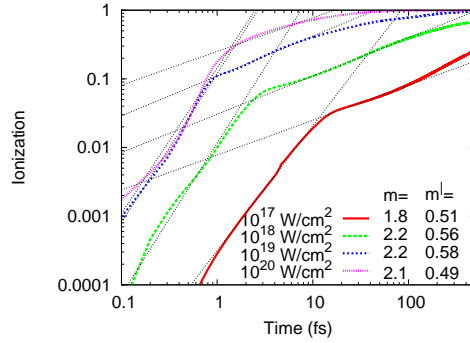


Fig. 1. Average ionization in carbon ions in a PSI crystal exposed to a 500 fs XFEL pulse, photon energy 6 keV. The thick lines represent the normalized average ionization (saturation at 1 corresponds to fully ionized atoms) and show two distinct regions which are fitted to a scaling law form $\sim t^m$ in the interval 0.1–1 fs and $\sim t^{m'}$ in the interval 1–10 fs, with t in fs (thin dotted lines). The average ionization for energies 2 keV, 9 keV and 12 keV can be found in the Appendix, Fig. 9.

plasma theory [60] is given by

$$D_i(t) = \frac{k_B T_i(t)}{m_i \nu_i(t)}, \quad (1)$$

where ν_i is the ion-ion collision frequency, T_i the ion temperature and m_i the mass. In the case of constant temperature and no ionization, the coefficient D is constant and as such describes Brownian motion. A solution to the diffusion equation gives the mean square displacement $\sigma^2(t) = 2NDt$, where N is the number of dimensions. For the case of a time-dependent coefficient $D_i(t)$ the diffusion equation is non-trivial to solve. Under the assumption that $D_i(t)$ is slowly varying with time (which is the case in these plasma simulations, except for the first few femtoseconds when plasma is getting formed), we can approximate the root mean square displacement (RMSD) $\sigma(t)$ for each time step t during the simulation

$$\sigma(t) = \sqrt{2N \int_0^t D_i(t') dt'}. \quad (2)$$

In the general case $N = 3$, however below we will calculate the displacement for the case of $N = 1$, since only the component of the atomic displacement along the direction of the momentum transfer q is relevant. Figure 2 shows the root mean square displacement as a function of time, calculated from simulations with various XFEL parameters (wavelength and intensities). The shape of the RMSD as a function of time is not strongly dependent on the intensity and could be represented by a scaling law $\sigma(t) = Bt^n$, with $n \sim 1.5 \pm 0.4$. Figure 10 in the Appendix illustrates broadly how the scaling law fits the displacement calculated from the simulations. For comparison, Brownian motion scales as \sqrt{t} . The atomic displacement will modulate the Bragg intensities depending on the scattering angle, which we describe in sec. 3.1.

Ionization and the occurrence of K-shell vacancies have a strong impact on the atomic scattering factor. Ionization of the outer shell electrons has more impact on the scattering at low scattering angles. The occurrence of single and double K-holes in the carbon atoms are illustrated in Fig. 3. For simplicity we only consider carbon atoms when we calculate how the scattered signal is affected by time-dependent changes in the electronic population. We note, however, that the other light atoms (nitrogen, oxygen) exhibit a similar ionization behavior.

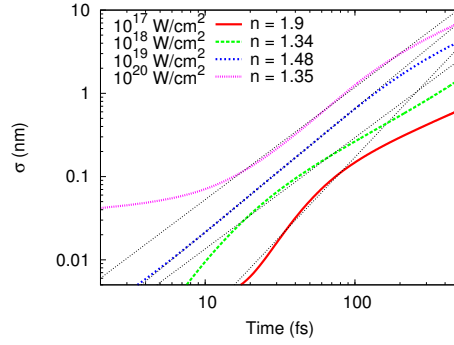


Fig. 2. Root mean squared displacement of the carbon ions in a PSI crystal exposed to a 500 fs XFEL pulse, photon energy of 6 keV. The thick lines represent the ion displacement which is fitted to a scaling law form $\sigma(t) = Bt^n$ in the interval 10–100 fs, with t in fs and B in units of nm/fs ^{n} (thin dotted lines). The RMSD for photon energies 2 keV, 9 keV and 12 keV can be found in the Appendix, Fig. 10.

3. Bragg signal decay due to ionization and ion displacement

The instantaneous scattered Bragg signal from a crystal exposed to a XFEL pulse decreases during the exposure due to the ionization and the displacement of the atoms, both leading to a loss of structural coherence. We assume these two phenomena can be described separately.

Consider a nanocrystal consisting of $N = n_1 \times n_2 \times n_3$ unit cells, of a molecule of M atoms. The total number of atoms in the nanocrystal is MN , excluding the solvent. The sample is in some random orientation and is illuminated by a short X-ray pulse. We assume the X-ray beam is collimated, and has an intensity at the sample of $I_0(t)$ photons per unit area per unit time. For a constant-intensity pulse of duration t_p , the pulse fluence is then $I_0 t_p$. Assuming that the coordinates of the MN atoms are $r_j(t)$ and scattering factors $f_j(t)$ at the time steps t during the pulse, at each instant of time t the diffraction pattern will be given by

$$I(q, t) = r_e^2 \Delta\Omega I_0(t) |F(q, t)|^2, \quad (3)$$

where $I(q, t)$ is the scattered intensity, q the inverse distance $q = 2 \sin(\theta)/\lambda$ (θ is the Bragg angle and λ wavelength), and

$$F(q, t) = \sum_{j=1}^{MN} f_j(t) e^{-2\pi i r_j(t) \cdot q}, \quad (4)$$

and $\Delta\Omega$ is the solid angle of each detector pixel.

3.1. Atomic displacement

We consider first the case of atomic motion without ionization. Following the derivation of Warren [21], the atomic trajectories are written as $r_i(t) = r_i^0 + \Delta_i(t)$, with $\langle \Delta_i(t) \rangle = 0$, averaged over all atom positions i , at any instant of time t . The r_i are the average positions and are equal to the positions of the undamaged perfect crystal.

The modulus squared of the time-dependent structure factor is then

$$|F(q, t)|^2 = \sum_i \sum_j f_i f_j e^{2\pi i q \cdot (r_i - r_j)} e^{2\pi i q \cdot (\Delta_i(t) - \Delta_j(t))}. \quad (5)$$

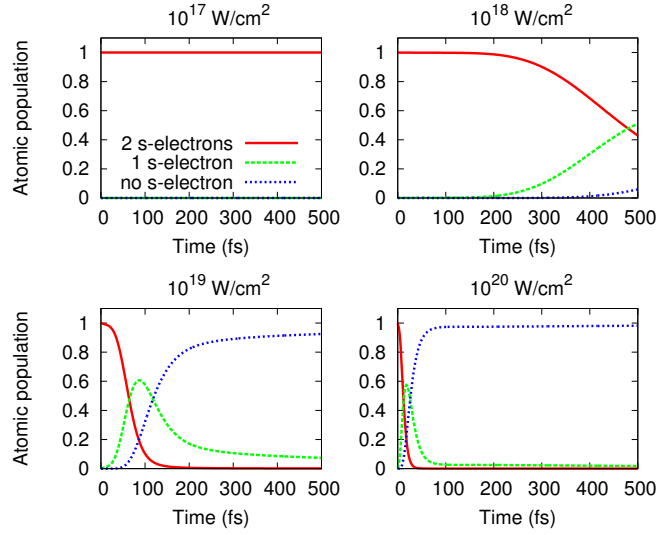


Fig. 3. Relative ion populations as a function of time for carbon atoms in a PSI crystal exposed to a 500 fs XFEL pulse, photon energy 6 keV. The populations are normalized to the total number of carbon atoms. The figure shows the states with a fully occupied K-shell including the neutral atoms (red line), all the ions with a K-shell vacancy (green line) and the ions with double vacancy in the K-shell, including the fully ionized carbon (blue line).

At any time t the displacements Δ_j are small and have equal probability of being in one direction or the opposite direction. We denote the variance of the distribution of displacements as $\sigma^2(t) = \langle \Delta^2(t) \rangle$, and assume for now that this is independent of the atomic species. We can then compute an average structure factor, assuming that the molecule is repeated in the crystal lattice and that each molecule has random perturbations of its atom positions

$$\langle |F(q, t)|^2 \rangle = N \sum_k^M f_k^2 \left(1 - e^{-4\pi^2 q^2 \sigma^2(t)} \right) + |F_0(q)|^2 e^{-4\pi^2 q^2 \sigma^2(t)}, \quad (6)$$

where the sum over k is over the M atoms of the molecule and $|F_0(q)|^2$ is the diffraction pattern of the entire perfect crystal of that molecule. This result is correct for small displacements, or for large displacements that are normally distributed. The first term in Eq. (6) is the diffuse scattering due to the unordered part of the structure, and is equal to the total incoherent scattering strength of the crystal multiplied with a term that increases with increasing q . The second term is the scattering from the mean structure which, since $\langle \Delta \rangle = 0$, is periodic. This is equal to the undamaged crystal diffraction pattern multiplied by an instant disorder factor (defined here as $h(q, t) = e^{-4\pi^2 q^2 \sigma^2(t)}$), which is similar to a Debye-Waller factor but is not governed by an equilibrium temperature. This filtering factor becomes smaller with higher resolution (increasing q).

The detector records the time-integrated diffraction pattern and assuming a flat-top pulse with $I_0(t) = I_0$ for $t < t_p$, we get for the Bragg scattering (neglecting the diffuse scattering term)

$$\begin{aligned} I_{\text{Bragg}}(q) &= I_0 r_e^2 \Delta\Omega |F_0(q)|^2 \int_0^{t_p} e^{-4\pi^2 q^2 \sigma^2(t)} dt \\ &= I_0 r_e^2 \Delta\Omega |F_0(q)|^2 \int_0^{t_p} h(q, t) dt. \end{aligned} \quad (7)$$

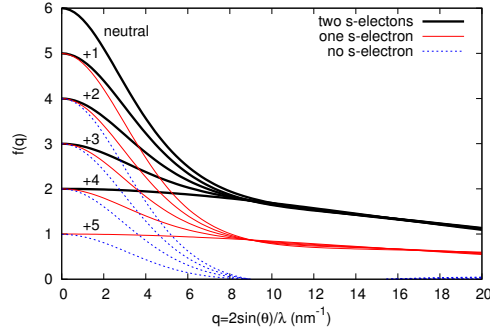


Fig. 4. Analytical approximations for the scattering factor $f(q)$ for the neutral and all ionized states of carbon, see Eq. (16). The figure shows collectively the form factors for the states with a fully occupied K-shell, half occupied K-shell and double K-shell vacancy in a carbon atom.

3.2. Ionization

The second case to consider is ionization of atoms without any atomic motion. Atoms are randomly ionized, and the electrons quickly become delocalized from the atomic position. The scattering factor of the ionized atom changes [61]. Figure 4 shows the atomic scattering factors for carbon in different electronic configurations. Consider a random occupancy of a fraction x of atoms with scattering factor f_0 and the rest $(1-x)$ with scattering factor f_1 . The average modulus squared of the time-dependent crystal structure factor is given by

$$\langle |F(q,t)|^2 \rangle = \sum_i \sum_j \langle f_i f_j \rangle e^{2\pi i(r_i - r_j)}, \quad (8)$$

which can be written as

$$\langle |F(q,t)|^2 \rangle = NMx(1-x)(f_0 - f_1)^2 + (x + (1-x)f_1/f_0)^2 |F(q,t)|^2. \quad (9)$$

As with Eq. (6), this is the sum of continuous diffuse scattering (first term) and reduced Bragg intensities (second term). However, in contrast to the case of atomic motion, the diffuse scattering (and reduction of Bragg scattering) has no q dependence. This is because there is no correlation between atoms ionized in one location to another location. The degree of diffuse scattering is a maximum when half the atoms are ionized, and is zero when all atoms are identical (none ionized or all ionized). For the macromolecular crystal, the ratio of Bragg diffraction to diffuse will be approximately

$$I_{\text{Bragg}}(q)/I_{\text{diff}} \approx \frac{(x + (1-x)f_1/f_0)^2}{NMx(1-x)} |F(q,t)|^2. \quad (10)$$

Considering a more general case, let us define m as a specific ionization state and x_m the fraction of atoms in ionization state m . The total number of elements in state m is then $MN x_m$. We further define f_m as the atomic form factor for ionization state m , Λ all the possible ionization states and

$$\langle f \rangle = \sum_{m=0}^{\Lambda} x_m f_m, \quad \sum_{m=0}^{\Lambda} x_m = 1, \quad (11)$$

$$f_m = \langle f \rangle + (1 - x_m) f_m - \sum_{n \neq m} x_n f_n. \quad (12)$$

This gives us a decrease in the scattering signal due to the ionization expressed as:

$$|F|^2 = \left| \sum_{i=0}^{M,N} \langle f \rangle e^{2\pi i q r_i} \right|^2 + 2 \sum_{m=0}^{\Lambda} MN x_m \langle f \rangle \left[(1-x_m) f_m - \sum_{n \neq m}^{\Lambda} x_n f_n \right] + \sum_{m=0}^{\Lambda} MN x_m \left[(1-x_m) f_m - \sum_{n \neq m}^{\Lambda} x_n f_n \right]^2, \quad (13)$$

where the first term,

$$\left| \sum_{i=0}^{M,N} \langle f \rangle e^{2\pi i q r_i} \right|^2 = \frac{\langle f \rangle^2}{\langle f_0 \rangle^2} |F_0(q)|^2, \quad (14)$$

is the Bragg scattering and the last two terms represent diffuse scattering. The degradation of the Bragg signal due to the ionization is therefore governed by

$$k(q, t) = \langle f \rangle^2 / \langle f_0 \rangle^2. \quad (15)$$

Our simulations keep track of the electronic population during the simulation, and using the method introduced by Cromer and Mann [62], we can estimate the atomic scattering factor for any possible ionization state

$$f(\sin(\theta)/\lambda) = \sum_{i=0}^4 a_i e^{-b_i (\sin(\theta)/\lambda)^2} + c, \quad (16)$$

where the parameters a_i, b_i and c are defined in Table 1 in the Appendix. Once $f(q)$ for each ionization state is calculated (shown in Fig. 4), these are weighted with the population of each state calculated for any time point during the simulation.

3.3. Total Bragg scattering decay

Assuming that the decrease in scattered signal due to displacement *and* ionization can be described in terms of two independent contributions, we can combine the findings from sections 3.1 and 3.2, and present an expression for the total Bragg scattering decay. The total (instantaneous) decrease in signal would then be described by $k(q, t)$, describing the ionization contribution, and $h(q, t)$ describing the contribution from the displacement. The time integrated (accumulated) Bragg signal then becomes

$$I_{\text{Bragg}}(q) = I_0 r_e^2 \Delta\Omega |F_0(q)|^2 \int k(q, t) h(q, t) dt = I_0 r_e^2 \Delta\Omega |F_0(q)|^2 \int \frac{\langle f \rangle^2}{\langle f_0 \rangle^2} e^{-4\pi^2 q^2 \sigma^2(t)} dt. \quad (17)$$

The behavior of I_{Bragg} is illustrated in Fig. 5. Based on the expressions derived in earlier sections, we can estimate the integrated (accumulated) Bragg signal in terms of scaling laws, in accordance with equations and the parameter fit from Fig. 1 and Fig. 2

$$I_{\text{Bragg}}(q) = I_0 r_e^2 \Delta\Omega |F_0(q)|^2 \int_0^{t_p} (1 - Et^m)^2 e^{-4\pi^2 q^2 Bt^{2n}} dt. \quad (18)$$

The dynamics due to ionization is described by the $(1 - Et^m)^2$ term, and the effect of the displacement by Bt^{2n} , where n and m are dependent on the dynamics as illustrated in Fig. 1 and Fig. 2. E and B are constants with typical values determined from simulations

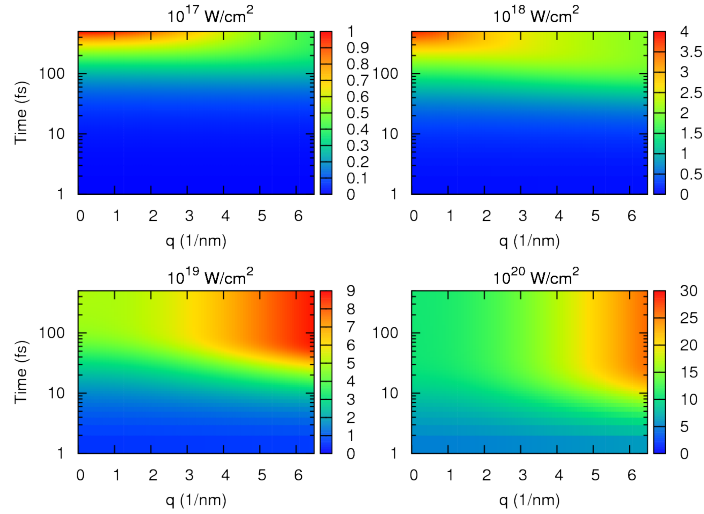


Fig. 5. Accumulated Bragg signal, $I_0 \times \int h(q,t)k(q,t)dt$, as a function of time during pulse t and resolution q for different intensities. The value for 6 keV and 10^{17} W/cm² is normalized to 1 to facilitate comparison with the different cases. Only ionization and displacement of carbon atoms are shown. The comparison with 2 keV, 9 keV and 12 keV is shown in the Appendix, Fig. 11.

$B = 10^{-3} \text{ nm}/(\text{fs})^{3/2}$ and $E = 0.1 \text{ fs}^{-2}$. This expression is presented as an analytical tool describing the time dynamics and can be used to estimate the scattered signal from a crystal due to ionization and atomic displacement. Figure 9 and Fig. 10 illustrate how well the approximate formulas for the ionization and displacement fit with the simulations.

4. Results and discussion

In conventional synchrotron crystallography the tolerable radiation dose for cryogenically cooled protein crystals is 30 MGy [29–31]. Figure 1 and Fig. 2 show that ionization and displacement depend strongly on the intensity, and hence the dose. The absorbed dose is proportional to incoming intensity only at lower intensities, Fig. 6. At high intensities, the absorbed dose is reduced with time, as the sample becomes more ionized and saturation to ionization sets in. The figure also shows that GGy doses can be achieved easily within 10 femtoseconds. Considering the radiation doses shown by our simulations, we conclude that the limit of 30 MGy does not apply to femtosecond X-ray nanocrystallography (this has also been pointed out in earlier experimental studies [6]). Instead femtosecond X-ray nanocrystallography can be used even at radiation dose rates that are orders of magnitude higher.

The occurrence of K-shell vacancies in the crystal has a direct effect on the scattering atomic factor. Figure 4 reveals that the low resolution information is much more sensitive to the ionization state than the high resolution information. At resolution $d = 0.1 \text{ nm}$ ($q = 10 \text{ nm}^{-1}$) the scattering factor is almost solely dependent on the number of s-electrons, whereas at $d = 0.5 \text{ nm}$ ($q = 2 \text{ nm}^{-1}$) it is much more dependent on the total number of bound electrons. To estimate the scattering at higher resolution it is therefore necessary to consider the occurrence of K-shell vacancies. In several of the simulated scenarios a large fraction of the carbon atoms have one or two s-electrons missing (vacancies), see Fig. 3.

The decrease in scattered Bragg signal (I_{Bragg}) originates from the loss of spatial coherence

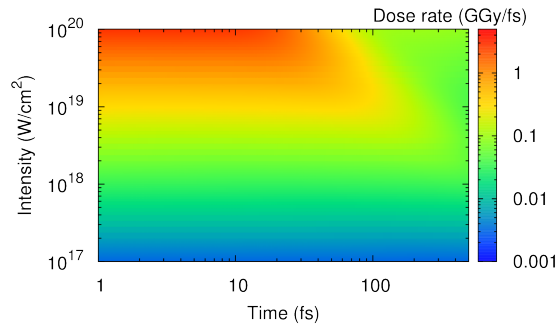


Fig. 6. Dose rate measured in GGy/femtosecond as a function of time during the pulse and incident intensity (photon energy is 6 keV). At higher intensities (above 10^{19} W/cm²), the absorbed dose is lower as the sample becomes transparent to the incident radiation.

due to both atomic displacements, described by $h(q,t)$ and ionization $k(q,t)$. The factor $k(q,t)$ is q -dependent mainly through the change in scattering form factors, and ionization dramatically reduces the scattering power at low q .

The factor $h(q,t)$ on the other hand, reduces the scattered signal starting at high q and moving towards lower q as the disorder in the crystal increases. In a sense the q dependence in $h(q,t)$ gives a direct measurement of the length scale of the displacement of the atoms in the sample—at least in the cases where the ionization is low. The two complementary damage processes affect the Bragg signals starting at different resolution regions, as illustrated in Fig. 5. Compare for example the simulations at 10^{17} W/cm² at 6 keV, where the ionization is low (on average 0.1 for carbon during the simulation), the signal is lost at high q , whereas for low q much more signal is accumulated. In the other extreme, at 10^{19} W/cm² where the carbon atoms are fully ionized within 100 fs, the high q Bragg peaks accumulate relatively more scattered photons. The overall signal is still higher at high intensities (10^{20} W/cm²) due to the high number of photons being scattered before the loss of coherence, as shown by the relative scale in Fig. 5.

Defining the time for the Bragg peak to reach 99% of its full intensity to be the time when the Bragg peak is "turned off", t_{off} , we display the fraction of the X-ray pulse that actually contributes to the signal in a Bragg peak in Fig. 7. For example, using a 2 keV pulse with 10^{20} W/cm², only a minute fraction of the pulse will contribute to Bragg peaks at an angle corresponding to a resolution of $d = 0.5$ nm ($q = 2$ nm⁻¹), the rest of the pulse will only contribute to the background. Exposing the sample to 10^3 times more intensity, does, at 12 keV, only increase the diffracted signal 180 times at $q = 5$ nm⁻¹. With a 10^{17} W/cm² pulse, about 60% of the 500 fs long pulse contributes to the Bragg scattered signal, whereas with a pulse with 10^{19} W/cm² only about 15% of the pulse is useful. Still, the maximum scattered signal at $q = 5$ nm⁻¹ is about 100 times higher in higher intensity pulse. Thus, the highest Bragg signal possible for achieving atomic resolution (for example at $q = 5$ nm⁻¹) would be achieved at 6 keV and highest possible intensity. At this given intensity, the pulse should be as short as possible, but longer than $t_{\text{off}} = 30$ fs, to reduce the diffuse signal.

Crystals as small as 10 unit cells in width have been measured at LCLS at a fluence of around 10^{17} W/cm² [4]. Depending on the crystal size and pulse intensity, diffraction beyond a resolution of 3 Å can easily be measured. For example, the $1 \times 1 \times 3$ μm³ lysozyme crystals measured by Boutet *et al.* contained about 200^3 unit cells on average and gave rise to measurable diffrac-

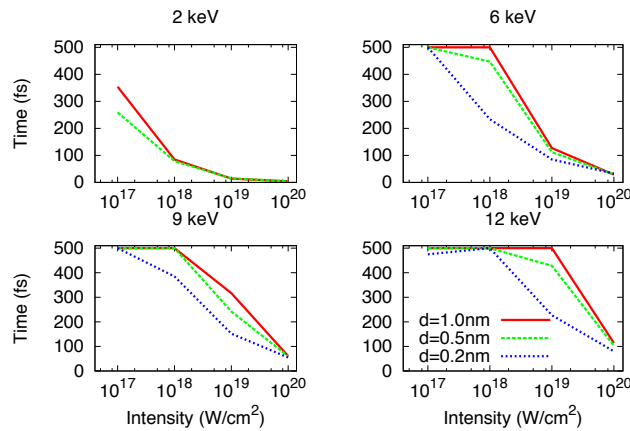


Fig. 7. Portion of pulse that contributes to the Bragg peak (t_{off}) for different resolutions, as a function of incident intensity. Shown are resolutions $d = 1 \text{ nm}$ ($q = 1 \text{ nm}^{-1}$), $d = 0.5 \text{ nm}$ ($q = 2 \text{ nm}^{-1}$) and $d = 0.2 \text{ nm}$ ($q = 5 \text{ nm}^{-1}$).

tion to 2 \AA at with pulses of fluence of 10^{17} W/cm^2 [7]. Smaller crystals can be measured at higher fluences, since the integrated Bragg signal scales with the number of unit cells in the crystal. The detectors used at the Coherent X-Ray Imaging instrument at LCLS, where most SFX experiments were performed so far, are capable to detect single photons and do not impose any limit to the achievable resolution.

In the future, as the XFEL sources get stronger and the focus gets tighter, the situation where the ionization plays an important role will be reached. The scattered Bragg signal at low resolution is sensitive to the electronic state of the ion. At high resolution the scattered signal is reduced due to ion displacement and the number of electrons in the K-shell. It has been shown earlier [6], that the so called Debye-Waller factor, which is routinely used as a correction factor in conventional synchrotron crystallography, will overcompensate high resolution peaks when compared to our Bragg termination model, even in cases where ionization can be assumed not to play a role. This correction factor will look very different for a situation with heavy ionization. In Fig. 8, the correction factors for our set of simulated parameters are displayed. With the 10^{17} W/cm^2 pulses, the correction factor is behaving Gaussian-like, but when the ionization becomes important, the shape changes drastically.

5. Conclusions

As X-ray free-electron lasers are becoming available to the macromolecular crystallography community, structural determination using small nano-sized crystals will likely become routine. The damage processes in nanocrystals illuminated by intense femtosecond X-ray lasers are different from the damage in conventional crystallography, due to the extreme high doses on the sample [2]. The ultra-intense pulses can ionize every atom in the sample, creating an exotic state of matter with hot free electrons which ultimately transfer energy into atomic motion, leading to loss of Bragg diffraction. This happens on time scales similar or shorter than the X-ray pulse, and hence it affects the scattered signal.

The decrease in Bragg signal is governed by two damage mechanisms; ionization leads to a lower scattering power of the atoms and atomic displacement leads to a breakdown of the crystalline structure. These processes have a different influence on the signal as a function of

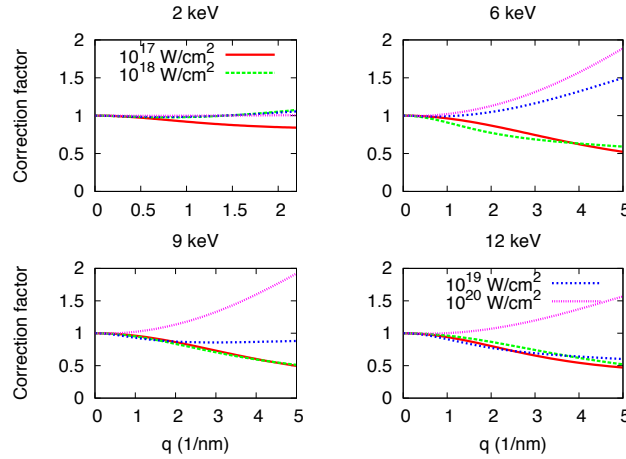


Fig. 8. Comparison of Bragg peak reduction at t_{off} normalized to 1 at $q = 0$. At low intensities the correction factor shows a Gaussian-like behavior, but for higher intensities the ionization plays an more explicit role, and the shape is far from Gaussian.

scattering angle, and hence resolution. The ionization dynamics shows an accelerated phase during the first femtoseconds of the pulse and dominates at high pulse intensities and affects the low resolution. At lower intensities, atomic displacement dominates the loss of coherence and gates the Bragg signal starting at high-resolution.

In the scenarios we have simulated the highest signal at high resolution ($d = 2 \text{ nm}$, $q = 10 \text{ nm}^{-1}$) is achieved using high intensity pulses and low energy photons (6 keV). The relevant variable which will influence imaging at high resolution is the incident photon intensity at the sample before the Bragg diffraction is gated, while the rest of the pulse will mainly contribute to background through diffuse scattering.

Appendix

We present extended versions of Fig. 1, Fig. 2 and Fig. 5, with simulations for photon energies of 2, 6, 9, and 12 keV, the table of the coefficients for the analytical approximation to the scattering factor and the average ion temperature in the simulations.

Table 1. Coefficients for the analytical approximation to the scattering factor $f(\sin(\theta)/\lambda) = \sum_{i=0}^4 a_i e^{-b_i(\sin(\theta)/\lambda)^2} + c$, for the carbon atoms and ions in different ionization state derived from [61].

ion state	a_1	b_1	a_2	b_2	a_3	b_3	a_4	b_4	c
$1s^2 2s^2 2p_x^1 2p_y^1$	2.310000	20.843899	1.020000	10.207500	1.588600	0.568700	0.865000	51.651199	0.215600
$1s^2 2s^2 2p_x^1$	-0.489731	8.4684	2.48822	12.8328	1.19572	33.0107	1.60467	0.541875	0.200401
$1s^2 2s^2$	-1.38165	14.1114	2.77209	13.9638	0.778653	33.0264	1.61321	0.577292	0.217136
$1s^2 2s^1$	-1.87258	8.44601	2.27916	8.44469	0.739724	25.2658	1.6246	0.608272	0.227395
$1s^2$	-1.98201	1.97109	2.16236	1.69624	0.46134	2.50755	1.23771	0.41756	0.120656
$1s^1$	0.375411	1.21437	0.0136561	4.22023	-0.00101152	10.39	0.560559	0.378494	0.0513822
$1s^1 2s^2 2p_x^1 2p_y^1$	2.77728	30.0853	-3.25577	-0.0404201	-0.854858	30.0945	2.34266	13.2072	3.98802
$1s^1 2s^2 2p_x^1$	2.15388	13.8341	-0.216291	3.13703	0.831943	0.517731	1.12941	33.5431	0.100378
$1s^1 2s^2$	0.755785	33.5168	1.44343	13.7656	0.808569	0.529178	-0.107225	4.0526	0.0989882
$1s^1 2s^1$	0.322141	35.4695	0.353258	0.0754788	0.692015	0.668296	0.754509	14.7044	-0.12205
$1s^0 2s^2 2p_x^1 2p_y^1$	-2.08507	5.57837	3.29061	8.4955	1.72713	31.0344	1.0113	18.2976	0.0539979
$1s^0 2s^2 2p_x^1$	-0.318757	5.16038	-0.663824	5.09891	2.27667	9.98617	1.66351	29.1491	0.0405806
$1s^0 2s^2$	0.443187	14.973	0.999582	30.037	-0.761219	5.22613	1.29023	8.91344	0.0271157
$1s^0 2s^1$	-0.00648436	0.980185	-0.0764447	1.03875	1.02365	19.9246	0.10077	0.140494	-0.0486892

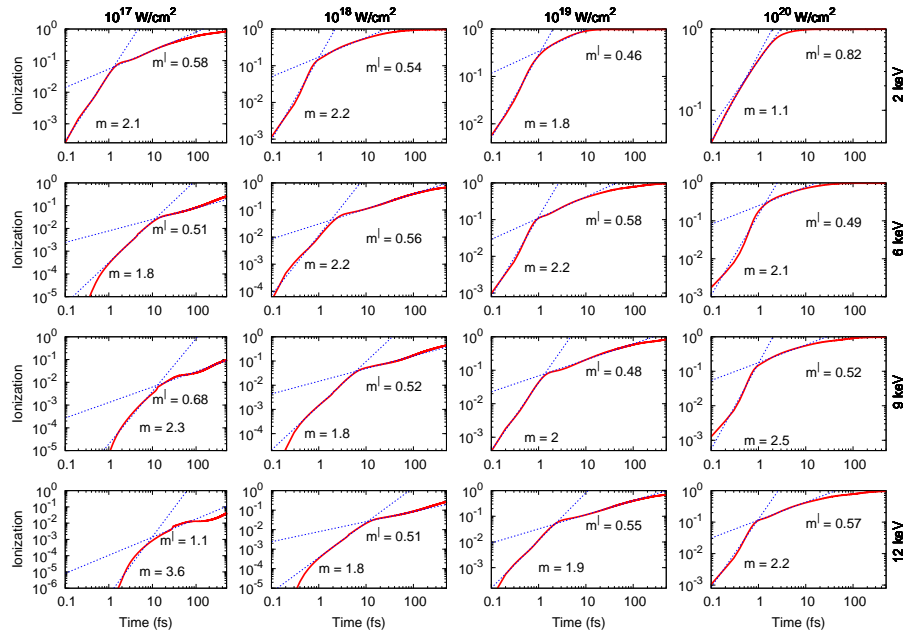


Fig. 9. Average ionization in carbon ions in a PSI crystal exposed to a 500 fs XFEL pulse. The solid red line represents the normalized average ionization (saturation at 1 corresponds to fully ionized atoms) and show two distinct regions which are fitted to a scaling law form $\sim t^m$ in the interval 0.1-1 fs and $\sim t^{m^l}$ in the interval 1-10 fs, with t in fs (blue dotted lines).

Acknowledgments

The authors thank the Helmholtz Association through the Center for Free-Electron Laser Science at DESY, Swedish Research foundation, Röntgen Ångström Cluster, and the Swedish Foundation for Strategic Research for financial support. The Swedish National Infrastructure for Computing, UPPMAX (project S00111-71 and p2012227) and David van der Spoel are acknowledged for computational resources, and Magnus Bergh for support with CRETIN simulations.

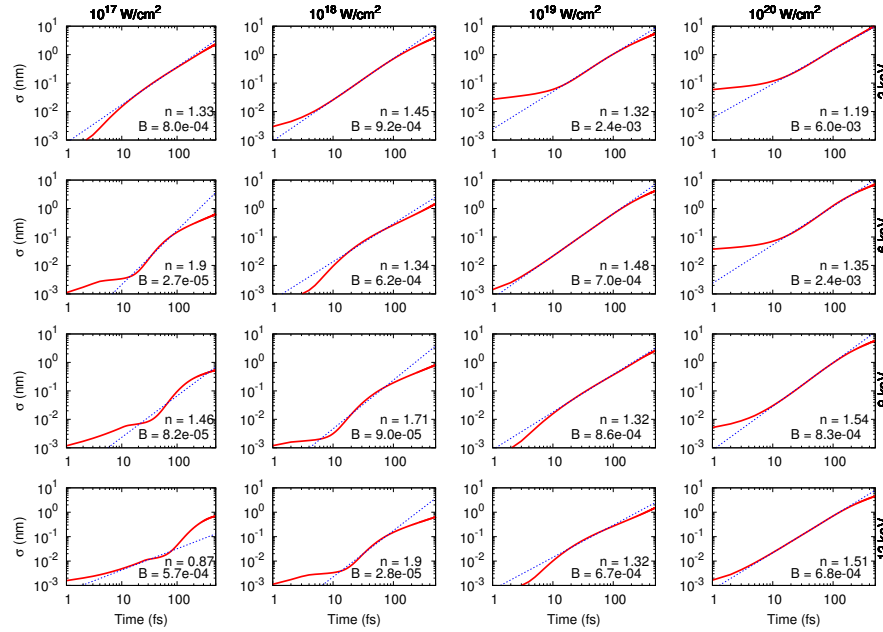


Fig. 10. Root mean squared displacement of the carbon ions in a PSI crystal exposed to a 500 fs XFEL pulse. The solid red line represents the ion displacement which are fitted to a scaling law form $\sigma(t) = Bt^n$ in the interval 10–100 fs, with t in fs and B in units of nm/fs^{*n*} (blue dotted line).

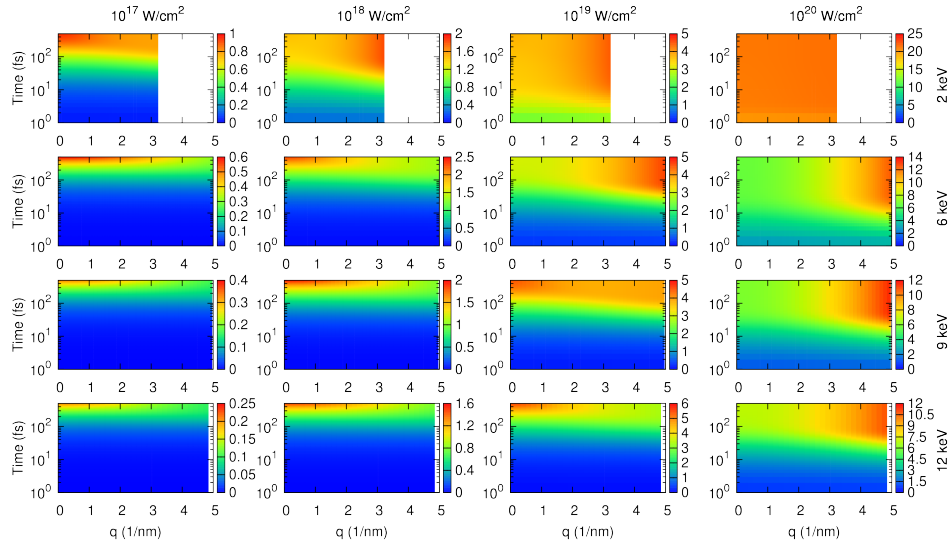


Fig. 11. Accumulated Bragg signal, $I_{\text{Bragg}} = I_0/\lambda^2 \times \int h(q,t)k(q,t)dt$, as a function of accumulation time and q . The result is normalized with XFEL intensity and photon wavelength λ^2 to facilitate a comparison of the expected signal between the different cases. The value for 2 keV and 10^{17} W/cm² is normalized to 1. Only ionization and displacement of carbon atoms are shown.

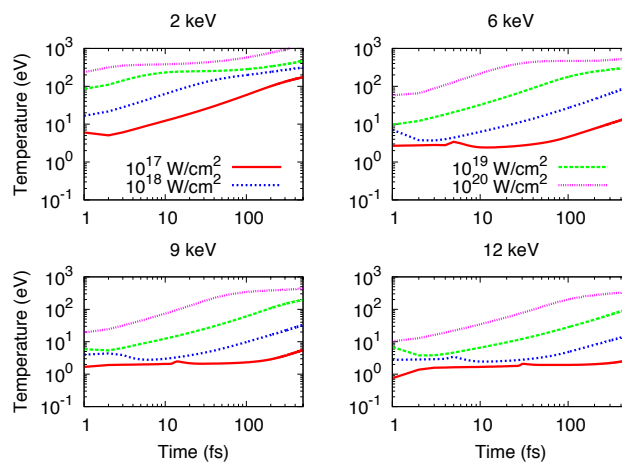


Fig. 12. Average ion temperature as a function of time, in a PSI crystal exposed to a 500 fs XFEL pulse, for different photon energies 2, 6, 9 and 12 keV, and various pulse intensities 10^{17} – 10^{20} W/cm². Only in the cases with very little ionization, the ion temperature is below the carbon-carbon bonding energy (about 1 eV) in the very beginning of the pulse. The plasma approximation is valid when the ion temperature in the system is above the average bond energy.